

Temperature-induced barium de-trapping from a double-well potential in $\text{Ba}_6\text{Ge}_{25}$

M. Schmidt, P. G. Radaelli, and M. J. Gutmann

ISIS Facility, Rutherford Appleton Laboratory, Chilton, Didcot, Oxon OX11 0QX, United Kingdom

S.J.L. Billinge

Department of Physics and Astronomy and Center for Fundamental Materials Research, Michigan State University, East Lansing, USA

N. Hur and S.W. Cheong

Department of Physics and Astronomy, Rutgers University, Piscataway, New Jersey 08854, USA

(Dated: November 20, 2018)

The crystal structure of barium-germanium clathrate $\text{Ba}_6\text{Ge}_{25}$ was studied using neutron powder diffraction in the temperature range 20–300K. The compound was found to be cubic (S.G. $P4_123$) in the entire temperature range. However, the fully-ordered model of the crystal structure (no split sites) is marginal at room temperature, and clearly fails at low temperature. A much better description of the crystal structure below 250K is given in terms of two split Ba sites, with random occupancies, for two out of three types of cages present in the $\text{Ba}_6\text{Ge}_{25}$ structure. The Ba atoms were found to interact strongly with the Ge host. The separation of the split Ba sites grows with decreasing temperature, with a sudden increase on cooling through the 200–250K temperature range, accompanied by an expansion of the entire crystal structure. We propose a simple model for this transition, based on temperature-induced de-trapping of Ba from a deep double-well potential. This transition is associated with sizeable anomalies in the transport and magnetic properties. The most significant of these effects, that is, the drop in electrical conductivity on cooling, can be easily explained within our model through the enhanced structural disorder, which would affect the relaxation time for all portions of the Fermi surface. We suggest that the other anomalies (increase in the absolute value of the negative Seebeck coefficient, decrease in the magnetic susceptibility) can be explained within the framework of the one-electron semi-classical model, without any need to invoke exotic electron-electron interaction mechanisms.

I. INTRODUCTION

There is growing interest in open-structure semiconducting materials that are considered promising candidates for thermoelectric applications. These compounds are characterized by low and often glass-like thermal conductivity κ , high electric conductivity σ and large Seebeck coefficient S . In particular, a significant research effort has focused on group III and IV clathrates, with heavy alkali metal, alkaline earth or rare earth guests. The group III and IV elements form a network of cages, in which a large atom is hosted. Usually, the guest atom is weakly bonded to the cage¹ and the sizes of cages are large enough for the atom to rattle. The semiconducting host can be doped to provide suitable electronic properties while the heavy guest atom can significantly lower the thermal conductivity of the material, due to resonant scattering of the heat carrying phonons^{2,3,4}, thereby increasing the thermoelectric figure of merit $Z = S^2\sigma/\kappa$. These materials are a realization of the “phonon glass, electron crystal” (PGEC) model proposed by Slack⁵.

The best-known materials of this class, such as $(\text{Ba}, \text{Sr}, \text{Eu})_8\text{Ga}_{16}\text{Ge}_{30}$, adopt the so-called type-I clathrate structure, which is also common to a variety of gas hydrates^{2,3,6}, and contains highly symmetric dodecahedral and tetrakaidecahedral cages^{3,7}. $\text{Ba}_6\text{Ge}_{25}$ is also a member of the clathrate family, but its crystal structure and its behaviour are unusual. $\text{Ba}_6\text{Ge}_{25}$ crystallizes in

the cubic $P4_132$ space group with a lattice parameter $a = 14.54536(7)$ Å and $Z = 4$. Barium occupies three non-equivalent crystallographic positions in the $\text{Ba}_6\text{Ge}_{25}$ unit cell^{8,9,10}. Ba(1) (8 equivalent sites per unit cell) is contained in distorted dodecahedral cages, sharing the pentagonal faces with each other and forms a spiral structure across the unit cell. However, Ba(2) (4 per unit cell) and Ba(3) (12 per unit cell) are hosted in channel-like structures that are interconnected throughout the unit cell^{8,9,10}. Another unusual structural feature is the fact that 32 out of 100 Ge atoms in each unit cell are three-coordinated, and accommodate a lone electron^{8,9,10}. The transport and magnetic properties of $\text{Ba}_6\text{Ge}_{25}$ are also unusual. Unlike $(\text{Ba}, \text{Sr}, \text{Eu})_8\text{Ga}_{16}\text{Ge}_{30}$, which can be prepared in both semiconducting and metallic form by slightly altering the Ga/Ge ratio, $\text{Ba}_6\text{Ge}_{25}$ is an n -type metal, with a fairly high carrier concentration ($n \sim 1\text{--}2 \cdot 10^{22}\text{cm}^{-3}$), and a good room-temperature electrical conductivity ($\sim 2000\Omega^{-1}\text{cm}^{-1}$)^{10,11}. The room-temperature Seebeck coefficient ($\sim -20\mu\text{V/K}$) is also consistent with metallic rather than semiconducting properties. Upon cooling below 240 K, $\text{Ba}_6\text{Ge}_{25}$ undergoes a transition, affecting the electrical conductivity (which decreases by almost a factor of 4), the Seebeck coefficient (which is negative and increases in absolute value) and the magnetic susceptibility χ , (which becomes more diamagnetic)¹¹. At low temperatures, $\text{Ba}_6\text{Ge}_{25}$ is still a metal, as clearly indicated by the linear temperature dependence of the specific heat and Seebeck coefficient,

and by the high carrier density, as determined by Hall effect measurements^{10,11}. Moreover, a superconducting transition has been discovered below 1 K¹².

This intriguing behaviour is clearly very difficult to understand with the naive Sommerfeld approach. In the free-electron model¹³, σ , S and the electronic (Pauli) component of the magnetic susceptibility χ_e are proportional to n , $n \pm 2/3$ and $n + 1/3$, respectively. σ is also proportional to the relaxation time τ , whereas the other two quantities are independent of τ . Qualitatively, one may conclude from the sign of the anomalies that a sharp reduction of the carrier concentration is occurring on cooling below the transition. However, recent Hall effect and specific heat measurements by Paschen *et al.*^{11,14} indicate that this is not the case. In fact, if the Hall measurements are interpreted in the simple single-band model, the drop in conductivity is almost entirely accounted for by a simultaneous drop in carrier *mobility* (which is proportional to τ). The interest in this compound has been further heightened by a report of a structural transition at the same temperature where the transport and magnetic anomalies occur. Although the crystallographic data are still unpublished, they are discussed in the aforementioned work by Paschen *et al.*¹¹ and used by Zerec *et al.*¹⁵ to calculate the electronic band structure of $\text{Ba}_6\text{Ge}_{25}$. The structural anomaly is not accompanied by a symmetry reduction. It is due to a strong increase of the Ba site disorder on cooling, and is consistent with the Ba atoms 'locking in' to two well-separated positions (split sites) at low temperatures. Paschen *et al.* speculate that the unusual transport and magnetic properties of $\text{Ba}_6\text{Ge}_{25}$ may arise from the formation of spinless bipolarons, whereby two carriers with opposite spins would dynamically stabilize a pair of Ba atoms separated by a short nearest-neighbour distance. Clearly, such a scenario may have important implications for understanding superconductivity in this system.

In this paper, we present detailed temperature dependent measurements of the $\text{Ba}_6\text{Ge}_{25}$ clathrate crystal structure, as determined from Rietveld refinements of neutron powder diffraction data in the temperature range 20–300K. The scattering contrast of Ge and Ba for neutrons ($b_{\text{Ba}}=3.86$ fm; $b_{\text{Ge}}=8.18$ fm) is reversed with respect to x-rays ($Z_{\text{Ba}}=56$; $Z_{\text{Ge}}=32$), providing a unique perspective not only on the large barium displacements, but also on the smaller displacements of the germanium framework. We conclude that, at low temperatures, Ba(2) and Ba(3) are trapped in a deep double-well potential, and that dynamic displacement coupled with electron hopping is very unlikely to occur. The trapping of barium atoms results in a dramatic structural rearrangement, which is bound to have a profound influence to the electronic states near the Fermi energy, especially those associated with narrow bands with predominant Ba character. Under these circumstances, the free-electron interpretation of the transport and magnetic properties clearly breaks down. However, we find that the single-electron (band) picture in the semi-clas-

sical approximation is most likely sufficient to describe this system, without any need to invoke exotic electron-electron interaction mechanisms.

II. EXPERIMENTAL

Polycrystalline $\text{Ba}_6\text{Ge}_{25}$ was prepared from elemental barium (99.2% purity, from Alfa Aesar) and germanium (99.999% purity, from Alfa Aesar) mixed together in the molar ratio of 1.15 : 4. Excess Ba was added to compensate for its evaporation from the reaction vessel. The mixture was placed in a closed graphite crucible, which was sealed in an evacuated silica ampoule. The reactants were slowly heated up to 1353K over a period of 10h and kept at this temperature for 8h. Then the sample was cooled down to room temperature over a period of 10h. The resulting sinter was black with brown tarnish layer on the surface. The brown impurity was washed away using methanol in an ultrasonic cleaner. The material was found to contain traces of graphite from the reaction crucible, as well as small traces of an unidentified phase. Neutron diffraction patterns were collected using the General Materials Diffractometer (GEM) at Rutherford Appleton Laboratory. The sample for the scattering experiment was enclosed in a vanadium can and attached to a closed cycle helium refrigerator. The measurements were carried out in the temperature range of 20–300K with 10K increments. At every temperature, data was acquired for 1h at 175 μA of proton beam current. The Rietveld analysis of the diffraction patterns was carried out using the GSAS package¹⁶. The crystal structure was visualized using ORTEP-3 program¹⁷.

III. STRUCTURE PROPERTIES

$\text{Ba}_6\text{Ge}_{25}$ was found to be cubic (space group P 4₁ 3 2) in the entire temperature range, with no trace of additional Bragg peaks at low temperatures. Preliminary Rietveld refinements were carried out using a model derived from room temperature x-ray single crystal experiments^{8,9,10}. In this paper we follow the atom labelling scheme of Kim *et al.*¹⁰.

Fig. 1 shows the a lattice parameter of $\text{Ba}_6\text{Ge}_{25}$ as a function of temperature. The lattice parameter increases with increasing temperature, but exhibits an anomaly in the 200–240K temperature range which indicates the phase transition in $\text{Ba}_6\text{Ge}_{25}$, as reported by Paschen *et al.*¹¹. The overall lattice expansion of $\text{Ba}_6\text{Ge}_{25}$ is $\Delta a = 0.018\text{\AA}$ ($\Delta a/a \approx 0.1\%$) in the 20–300K temperature range. It should also be noted that the lattice parameter contraction associated with the anomaly is very small (0.004 \AA). In our data the contraction happens smoothly over a 40 K range. This smooth cross-over is also reflected in our measurements of resistivity (see inset in Fig. 1) and contrasts with the sharp cross-over reported by Paschen *et al.*¹¹. These authors report

a transition with first-order character, accompanied by hysteresis.

The atomic displacement parameters (ADP's) of Ba(2) and Ba(3) at room temperature were found to be large and anisotropic as previously reported^{9,10}. A refinement of the low temperature patterns produced even larger displacements, increasing with decreasing temperature. This behaviour clearly indicated that the room temperature model is not adequate for the low temperature structure. The Ba(2) and Ba(3) sites were examined using difference Fourier maps. The maps present the difference between the experimental data and the model with an empty Ba site. The results for 20K, 200K, 240K and 300K are presented in Fig. 2. The low temperature nuclear density distribution maps (20K) clearly show the tendency of Ba(2) and Ba(3) atoms to move away from the site centre. This effect is especially pronounced in the case of the Ba(3) site. The site separation increases with decreasing temperature. Inspection of the maps shows that the splitting of the Ba(2) site virtually disappears above 240K but the Ba(3) site still shows signs of the site separation up to 300K. Multiple rattler sites were observed in Sr and Eu bearing type-I clathrates ($\text{X}_8\text{Ga}_{16}\text{Ge}_{30}$) but not in the Ba isomorph^{2,3,4,7}. This effect was accommodated in the current model by splitting the Ba(2) and Ba(3) sites along the direction of the largest thermal displacement at all temperatures. The symmetry of the Ba sites was reduced as follows: Ba(2) 4a \rightarrow 8c; Ba(3) 12b \rightarrow 24e. The split Ba site occupancies were reduced to 0.5 to maintain the overall stoichiometry. Using this model the refinement produced sensible thermal displacement of Ba atoms. At room temperature, the two models are almost equivalent, but, for consistency, we chose to carry out all the refinements using the split-site model. Sets of refined atomic coordinates and Debye-Waller factors at 20K and 300K are presented in Tables 1-2. An example of a refined pattern is shown in Fig. 3.

IV. BOND GEOMETRY

As the $\text{Ba}_6\text{Ge}_{25}$ crystal structure is complex, its analysis becomes easier by focusing on the Ge framework and on its individual building blocks (cages), bearing in mind that the cages share faces with each other and changes to a single Ge-Ge bond length affects all the cages. As already mentioned, the case of $\text{Ba}_6\text{Ge}_{25}$ is unusual as the movement of Ba atoms also affects the Ge framework.

A. Ge framework

All Ge-Ge bonds in the $\text{Ba}_6\text{Ge}_{25}$ structure are longer than in the elemental Ge (2.45Å). The Ge(1)-Ge(5) (equal to 2.48Å and 2.54Å) and Ge(4)-Ge(4)=2.47Å (the latter belongs to Ba(3) cage discussed below) distances are constant with temperature and are the shortest in

the Ge network. All other Ge-Ge bonds with the exception of Ge(2)-Ge(3) and Ge(1)-Ge(6) monotonically increase with temperature within the range 2.535–2.615Å as expected from thermal expansion. The Ge(2)-Ge(3) and Ge(1)-Ge(6) bond lengths are presented in Fig. 4 as functions of temperature. These bonds are almost constant below 100K and above 250K and change between 100K and 250K, with maximum derivative in the 200–240K temperature range, corresponding to the magnetic and transport anomalies¹¹. The transition also leads to small (less than one degree) changes in Ge-Ge-Ge angles associated with three-coordinated germaniums.

B. Ba(1) cage

The local environment of Ba(1) is presented in Fig. 5. Ba(1) is contained in a distorted dodecahedral cage with a 3-fold symmetry axis. Ba(1) cages share the pentagonal faces with other Ba(1) and Ba(3) cages and form a spiral structure in the crystal. Ba(1) together with Ge(4) and Ge(6) are located on the 3-fold axis, which is also the direction of their largest thermal displacement. The Ba(1)-Ba(1) nearest neighbour distance increases with temperature from 5.43Å at 20K to 5.46Å at 300K and does not show any signs of transition. The shortest Ba(1)-Ge(2) \approx 3.5Å and Ba(1)-Ge(5) \approx 3.4Å bonds are constant with temperature and the Ba(1)-Ge(1) shortest distance increase with temperature from 3.42Å at 20K to 3.46Å at 300K. These are the shortest Ba(1)-Ge bonds in the Ba(1) cage. Their value suggests that Ge(1), Ge(2) and Ge(5) are at contact distance from Ba(1). The environment of Ba(1) seems to be the same as in the type-I clathrates (the lengths are the same as calculated for $\text{Ba}_8\text{Ga}_{16}\text{Ge}_{30}$ cages)¹. The remaining Ba(1)-Ge bonds change with temperature within the range 3.470–3.935Å.

The reduction of Ge(2)-Ge(3) distance described above leads to a step like reduction of the Ba(1)-Ge(3) and Ba(1)-Ge(4) distances, as shown in Fig. 6. The increase of the Ge(1)-Ge(6) bond causes the Ge(6) atom to move away from Ba(1) (see Fig. 6). However, the Ba(1)-Ge(6) increase is greater than Ba(1)-Ge(4) decrease so the entire Ba(1) cage expands along 3-fold axis by 0.03Å over the 20–300K temperature range. The length of the Ba(1) cage along the 3-fold axis is presented in Fig. 7 as a function of temperature.

C. Ba(2) cage

The Ge(3) and Ge(6) atoms form a pseudo-cubic environment of Ba(2) presented in Fig. 5. Ge(6) and Ba(2) lie on the 3-fold axis of the unit cell and triplets of Ge(3) atoms on both sides of Ba(2) form equilateral triangles rotated almost 60° with respect to each other. Each Ba(2) cage is connected to six Ba(3) cages and together form channels in the crystal structure. It should be noted that only one of the split Ba sites is occupied at a time.

On average, each of the wells is occupied with 50% probability. From our data, no long-range correlation between occupied sites can be detected, since no superlattice Bragg reflections are observed at low temperatures. However, the possibility of short-range ordering, leading, for example, to the formation of clusters of Ba^{2+} ions, could not be ruled out. This aspect is currently being investigated by means of diffraction techniques that are sensitive to the local structure.

The distance between the split Ba(2) sites is presented in Fig. 8 as a function of temperature. The separation of Ba atoms is constant up to 100K then starts to decrease and rapidly falls in the 200–250K range. This sudden decrease in the Ba(2)-Ba(2) site distance coincides with the kink in the lattice parameter (see Fig. 1). The shape of this curve closely follows the shape of the $\text{Ba}_6\text{Ge}_{25}$ resistivity curve of Paschen *et al.*¹¹. At room temperature the split Ba(2) sites remain separated by 0.4Å.

The Ba(2)-Ge(3) bonds, marked with solid lines in Fig. 5, are constant up to 200K ($\sim 3.31\text{\AA}$) and increase to 3.34Å in the 200–250K temperature range. The almost constant value of the distance suggests a bonding of the three-coordinated Ge(3) with Ba(2) or a close contact of both atoms. These lengths are characteristic for Ba-Ge bonds observed in other Ba-Ge intermetallics^{18,19,20,21,22}. The Ba(2)-Ge(6) distance is too large ($> 3.6\text{\AA}$) for Ge(6) to form a bond with Ba(2). The length of the Ba(2) cage along the 3-fold axis is presented in Fig. 7 as a function of temperature. Its size decreases by $\sim 0.06\text{\AA}$ at the phase transition.

D. Ba(3) cage

The Ba(3) atom is contained in a heavily distorted dodecahedral cage presented in Fig. 9. This cage is the largest in the $\text{Ba}_6\text{Ge}_{25}$ structure and has 2-fold symmetry with the rotation axis bisecting the Ge(1)-Ge(1) and Ge(4)-Ge(4) bonds. As in the case of Ba(2) cage, only one of the split Ba sites is occupied; the distance between the split sites is shown in Fig. 8 as a function of temperature. The Ba(3) site separation exhibits similar behaviour to the Ba(2) site in the same temperature region. However the room temperature separation distance is equal to 0.56Å. Fig. 10 shows the Ba(2) site separation as a function of the Ba(3) site separation. The displacement amplitudes of Ba atoms in both cages are clearly correlated. However, the straight line fitted to the data does not cross the origin of the plot. Its negative offset indicates that Ba(3) atom can still be displaced from the cage centre while Ba(2) atom remains in the centre of its cage. This is consistent with the Fourier maps presented in Fig. 2.

The shortest Ba(3)-Ge distances are again formed by three coordinated Ge(3) and Ge(6) atoms. The Ba(3)-Ge(3) $\approx 3.3\text{\AA}$ and Ba(3)-Ge(6) $\approx 3.43\text{\AA}$ distances are constant. The remaining Ba(3)-Ge bonds are greater than 3.45Å and vary with temperature. Once again, this sug-

gests close contact of Ba and Ge atoms.

As indicated above the split site model yields acceptable temperature dependence of Ba thermal parameters, see Table 2. The thermal displacement of Ba(2) and Ba(3) is the largest among all atoms and their temperature dependence shows signs of the transition. This is most likely due to contraction of the Ge host in the 200–240K temperature range, which constricts the thermal movement of the rattlers. Also Ge(6) exhibits a substantial but constant thermal displacement along the 3-fold axis. This 3-coordinated Ge atom exhibits large thermal displacement because of the geometry of the lattice. Ge(6) is coordinated to three Ge(1) atoms but large distance to Ba(1) and Ba(2) along the 3-fold axis (see discussion above) allow it to move freely.

E. Concluding remarks

The introduction of the split sites in Ba(2) and Ba(3) cages leads to a minimum Ba(2)-Ba(3) distance. The shortest distance between Ba(2) and Ba(3) is presented in Fig. 11 as a function of temperature. The Ba(2)-Ba(3) closest distance is of the same order as in the elemental Ba (4.35Å). It seems that Ba atoms can interact with each other, which is consistent with theoretical predictions¹.

V. DISCUSSION AND CONCLUSIONS

The results of the previous sections can be summarised as follows: we have observed clear changes in both lattice and internal structural parameters, associated with the well-known anomalies in the transport and magnetic properties of $\text{Ba}_6\text{Ge}_{25}$. The most remarkable structural change is the displacement of Ba(2) and Ba(3) away from their high-symmetry site, thereby forming a two-fold split site occupied in a random way with 50% probability. This splitting may already be present at room temperature, but is greatly enhanced on cooling, with a sudden increase through the transition. We have also evidenced significant changes in the Ge framework at the transition. Interestingly, the most significant framework distortions affect the position of Ge(3) and Ge(6) (through the Ge(2)-Ge(3) and Ge(1)-Ge(6) bond lengths and associated bond angles). Ge(3) and Ge(6) are both 3-coordinated and both form close-contact distances with Ba(2) and Ba(3). Based on this scenario, we will attempt to relate the observed structural changes to the known anomalies in the transport and magnetic properties; in particular, we will focus on three main questions: 1) What is the driving force for the Ba-site splitting on cooling? 2) What is the likely effect of this distortion on the electronic structure, and is this sufficient to explain the observed anomalies? 3) Is there any need to go beyond the one-electron approximation? Question number 3 is particularly relevant in the light of the spinless bipo-

laron mechanism proposed by Paschen *et al.*¹¹ to explain the drop in magnetic susceptibility, and of the observation of superconductivity in this system below 1 K¹².

A. Mechanism of the structural transition

The simplest mechanism for explaining the observed behaviour of the Ba(2) and Ba(3) sites is that of temperature-induced de-trapping from a symmetric double-well potential; this is a purely 'geometrical' effect, which would take place within a rigid framework and, in its simplest form, does not depend on the conduction electrons. In this case, the close-contact interaction between Ba and the 3-fold-coordinated Ge atoms (Ge(3) and Ge(6)) would provide both the attractive and the repulsive components of the potential. A quartic potential bounded on both sides by infinite walls provides the simplest implementation of this model (Fig. 12), which can be solved numerically in both classic and quantum cases. Qualitatively, the physics of this model is easy to understand and is in agreement with the observations: at low temperatures, Ba(2) and Ba(3) are statistically trapped in one of the two wells of a symmetric double-well potential. On warming, the atoms explore the available levels within each well, but remain confined until their energy becomes comparable with that of the central maximum. When the thermal energy becomes comparable to the barrier height, the atoms are 'de-trapped', and become free to jump between wells and to occupy the central position with finite probability. Quantitatively, the quartic potential model is able to explain only about 30% of the change in Ba-Ba split distances, but larger changes can be obtained by using more realistic potentials²³. Irrespectively of the details of the potential, the main drawback of this model is that it only produces smooth crossovers through the de-trapping temperature, and is therefore unable to describe a first-order transition as observed by Paschen *et al.*¹¹. However, we have clearly shown that the Ge framework distorts in a significant way through the transition, and it is conceivable that the Ba-Ge interaction could modify the character of the transition. In spite of these difficulties, we are persuaded that the key to understand the structural transition is the formation of symmetric double-well potential at the Ba(2) and Ba(3) sites. The role of frustration in preventing a collective structural distortion also deserves to be investigated.

B. Consequence of the structural transition on the electronic structure

At low temperature the Ba(2) and Ba(3) ions are displaced; however, no superlattice peaks are evident therefore the displaced sites must be occupied in a random, or short-range ordered, fashion. We would like to examine the possible effect of this on the electronic and

transport properties. We have shown that structural changes occur for both the Ba sites and the Ge framework, strongly suggesting that the disorder will result in increased scattering for bands with both Ba and Ge predominant character. This observation, by itself, is sufficient to explain the drop of carrier mobility on cooling, which would be a consequence of the reduced mean free path for the conduction electrons. However, the observation of anomalies in both the Seebeck coefficient and the magnetic susceptibility clearly indicate that changes in the electronic structure at the Fermi surface are taking place through the transition. If we abandon the naive free-electron model and write S and χ_e in the semiclassical one-electron model¹³ we obtain:

$$S = -\frac{\pi^2}{3} \left(\frac{k_B}{e} \right) k_B T \frac{\partial \log \sigma(E)}{\partial E} \Big|_{E_F},$$

$$\chi_{Pauli} = \mu_B^2 g(E_F)$$

where $\sigma(E) = e^2 \tau(E) g(E) \frac{1}{3} v(E)^2$ is the generalised conductivity, $\tau(E)$ is the relaxation time, $g(E)$ is the density of states (DOS) and $v(E)$ is the electron velocity (which we considered isotropic for simplicity; all terms are formally energy-dependent). The observations are consistent with an overall *reduction* of the DOS and an increased *asymmetry* of the generalised conductivity through the Fermi surface. Clearly, we would not expect the broad and relatively featureless bands originating from the Ge framework to display such behaviour. However, recent band structure calculations by Zerec *et al.*¹⁵ have identified the presence of narrow bands with predominant Ba character, which cross the Fermi surface for the undistorted model and are significantly affected by off-site Ba displacement. These band need not contribute greatly to either the overall conductivity or the carrier density, as speculated by Zerec *et al.*¹⁵, as long as one still assumes that enhanced disorder is the main driving force for the resistive anomaly. In summary, the observed changes in transport and magnetic properties can be explained by a reduced relaxation time at low temperatures and a change in the Ba-related bands at the Fermi surface, both effects being consistent with the observed structural behaviour.

C. The spinless bipolaron scenario

Based on the previous considerations, there seems to be no need for additional mechanisms involving strong electron-electron correlation, as proposed by Paschen *et al.*¹¹. In particular, in the temperature-induced de-trapping scenario, Ba displacement would occur spontaneously, without the need to be associated with a single or a pair of localised electrons. This is not to say that polaron physics is not relevant for this material, since there is clearly strong coupling between the lattice and the conduction electrons. However, low-temperature electronic transport associated with 'jumps' of Ba atoms between different wells, as proposed by Paschen *et al.*¹¹, is highly unlikely. This can be shown in a simple manner by estimating the Ba tunneling rate, $\Gamma = \Gamma_0 e^{-2\lambda}$, where $e^{-\lambda}$

is the overlap between wavefunctions in the double well, Γ_0 is a typical phonon frequency and $\lambda \approx \frac{1}{2} \sqrt{\frac{2mV_0}{\hbar^2}}$.²⁴ Here, V_0 is the barrier height and m is the mass of the tunnelling atom. By setting $V_0 = 20$ meV (i.e., of the order of the transition temperature), $\Gamma_0 = 5 \times 10^{12}$ sec⁻¹ and $m = 137m_p$ we get $\lambda = 14.5$, $\Gamma = 0.2$ sec⁻¹. In other words, the tunnelling rate is macroscopically slow, as expected for heavy atoms such as barium. Therefore, we believe that the low-temperature disorder is essentially *static*, and cannot be associated with electron hopping. On this point, we make a final consideration: multi-well sites in type-I clathrates were previously associated with glass-like thermal conductivity^{2,3,4,7}, through a tunnel-like mechanism. The observation of a crystal-like thermal conductivity in Ba₆Ge₂₅, which displays multi-well Ba sites, calls for this proposal to be re-examined. Moreover, one should seriously question whether the tunnelling rates for these heavy-atom systems are sufficiently fast to affect low-temperature heat and electronic transport.

D. Conclusions

We have determined the crystal structure of the Ba₆Ge₂₅ clathrate as a function of temperature between 20 and 300K by neutron powder diffraction data. Although the structure was found to be cubic (space group P 4₁ 3 2) at all temperatures, the fully-ordered structural model^{8,9,10} fails to describe the data, particularly at low temperatures. Much better fits are obtained by modelling the nuclear density for two out of the three barium positions (Ba(2) and Ba(3)) with statistically occupied split sites. Ba₆Ge₂₅ was found to undergo a significant structural rearrangement around 240K. Although the main effect at the transition is an increase of the distance between split Ba sites on cooling, we have observed significant changes in some of the Ge-Ge bond lengths and angles, indicating strong interactions between the Ba

atoms and the Ge framework. The observed structural behaviour can be explained in a simple way by assuming that Ba(2) and Ba(3) are trapped, at low temperatures, within a deep double-well potential, from which they escape when their thermal energy becomes comparable to the barrier height. From our data, the transition appears to be continuous, but the character of the transition is likely to be sample-dependent; other data¹¹ suggest a first-order character, which would require a significant involvement of the Ge framework in the de-trapping process. As far as transport and magnetic properties are concerned, the main consequence of the transition is the enhanced structural disorder on cooling, which is likely to affect significantly all parts of the Fermi surface. This mechanism provides a natural explanation for the drop in electrical conductivity through the transition. The other transport and magnetic anomalies (increase in the absolute value of the negative Seebeck coefficient, decrease in the magnetic susceptibility) can be explained within the framework of the one-electron semi-classical model, by assuming that Ba contributes with narrow bands at the Fermi surface, as confirmed by recent band structure calculations¹⁵. Electron-phonon interaction is likely to be strong in Ba₆Ge₂₅, which may explain the observation of superconductivity below 1 K¹². However, we argue that Ba-site disorder is probably static at low temperatures, suggesting that polaron hopping involving Ba inter-well jumps is unlikely to contribute to the electrical or thermal conductivity.

VI. ACKNOWLEDGEMENTS

This work was supported in part by US DOE Office of Science grant DE-FG02-97ER45651. Reproduction of this article, with the customary credit to the source, is permitted. We are grateful to Daniel Khomskii, Alex Shluger and Laurent Chapon for discussing with the authors the results of this work.

-
- ¹ N. P. Blake, D. Bryan, S. Lattturner, L. Møllnitz, G. D. Stucky, and H. Metiu, *J. Chem. Phys.* **114**, 10063 (2001).
 - ² G. S. Nolas, T. J. R. Weakley, J. L. Cohn, and R. Sharma, *Phys. Rev. B* **61**, 3845 (2000).
 - ³ B. C. Sales, B. C. Chakoumakos, R. Jin, J. R. Thompson, and D. Mandrus, *Phys. Rev. B* **63**, 245113 (2001).
 - ⁴ V. Keppens, B. C. Sales, D. Mandrus, B. C. Chakoumakos, and C. Laermans, *Phil. Mag. Lett.* **80**, 807 (2000).
 - ⁵ G. A. Slack, *CRC Handbook of Thermoelectrics* (Chemical Rubber Company Boca Raton, FL, 1995), chap. 34, pp. 407–440.
 - ⁶ L. Pauling and R. E. Marsh, *Proc. Nat. Acad. Sci. U. S. A.* **38**, 112 (1952).
 - ⁷ B. C. Chakoumakos, B. C. Sales, D. G. Mandrus, and G. S. Nolas, *J. Alloys Compounds* **296**, 80 (2000).
 - ⁸ W. Carrillo-Cabrera, J. Curda, H. G. von Schnering, S. Paschen, and Y. Grin, *Z. Kristall. NCS* **215**, 207 (2000).
 - ⁹ H. Fukuoka, K. Iwai, S. Yamanaka, H. Abe, K. Yoza, and L. Haming, *J. Solid State Chem.* **151**, 117 (2000).
 - ¹⁰ S.-J. Kim, H. Siqing, C. Uher, T. Hogan, B. Huang, J. D. Corbett, and M. G. Kanatzidis, *J. Solid State Chem.* **153**, 321 (2000).
 - ¹¹ S. Paschen, V. H. Tran, M. Baenitz, W. Carrillo-Cabrera, Y. Grin, and F. Steglich, *Phys. Rev. B* **65**, 134435 (2002).
 - ¹² F. M. Grosche, H. Q. Yuan, W. Carrillo-Cabrera, S. Paschen, C. Langhammer, F. Kromer, G. Sparn, M. Baenitz, Y. Grin, and F. Steglich, *Phys. Rev. Lett.* **87**, 247003 (2001).
 - ¹³ N. W. Ashcroft and N. D. Mermin, *Solid State Physics* (Holt, Rinehart and Winston, 1976).
 - ¹⁴ F. Steglich, A. Bentien, M. Baenitz, W. Carrillo-Cabrera, F. Grosche, C. Langhammer, S. Paschen, G. Sparn,

- V. Tran, H. Yuan, et al., *Physica B* **318**, 97 (2002).
- ¹⁵ I. Zerec, A. Yaresko, P. Thalmeier, and Y. Grin, *Phys. Rev. B* **66**, 045115 (2002).
 - ¹⁶ A. C. Larson and R. B. von Dreele, Tech. Rep. LAUR 86-748, Los Alamos National Laboratory (2000).
 - ¹⁷ L. J. Farrugia, *J. Appl. Cryst.* **30**, 565 (1997).
 - ¹⁸ K. Turban and H. Schaefer, *Zeitschrift fuer Naturforschung, Teil B. Anorganische Chemie, Organische Chemie* **28**, 220 (1973).
 - ¹⁹ J. Evers, G. Oehlinger, and A. Weiss, *Zeitschrift fuer Naturforschung, Teil B. Anorganische Chemie, Organische Chemie* **35**, 397 (1980).
 - ²⁰ J. T. Vaughey, G. J. Miller, S. Gravelle, E. A. Leon-Escamilla, and J. D. Corbett, *J. Solid State Chem.* **133**, 501 (1997).
 - ²¹ R. Kroener, K. Peters, and H. G. von Schnering, *Z. Kristallogr. NCS* **213**, 662 (1998).
 - ²² F. Zuercher and R. Nesper, *Angew.Chem.,Int.Ed.Engl.* **37**, 3314 (1998).
 - ²³ P. G. Radaelli, unpublished (????).
 - ²⁴ P. W. Anderson, B. I. Halperin, and C. M. Varma, *Philosophical Magazine* **25**, 1 (1972).

VII. FIGURE CAPTIONS

Fig. 1 The cubic lattice parameter of $\text{Ba}_6\text{Ge}_{25}$ as a function of temperature. The error bars mark the standard deviation obtained from refinement. The inset shows the specific resistivity of $\text{Ba}_6\text{Ge}_{25}$ as a function of temperature.

Fig. 2 Nuclear density at the Ba(2) and Ba(3) sites for $\text{Ba}_6\text{Ge}_{25}$ at 20K, 200K, 240K and 300K in difference Fourier maps determined from powder diffraction. The maps present the difference between the experimental data and the model with an empty Ba site. The size of all maps is $5 \times 5 \text{ \AA}^2$.

Fig. 3 An example of a refined $\text{Ba}_6\text{Ge}_{25}$ diffraction pattern from the 63° bank. The figure shows the observed intensities (circles), calculated pattern and the difference curve (solid lines). The top and bottom rows of tick marks indicate the positions of graphite and clathrate Bragg reflections respectively. The strongest line of the

unidentified impurity is visible at 3.25 \AA of d-spacing.

Fig. 4 The Ge(1)-Ge(6) and Ge(2)-Ge(3) bond lengths in $\text{Ba}_6\text{Ge}_{25}$ as a function of temperature. The lines are guide for eye.

Fig. 5 Local environments of Ba(1) and Ba(2) sites in $\text{Ba}_6\text{Ge}_{25}$ at 20K derived from Rietveld refinement. The Ba(1) resides inside of the distorted dodecahedral cage (Ba atom not shown). The cage has got 3-fold symmetry with the Ge(4), Ge(6) and Ba(1) lying on the rotation axis. The environment of Ba(2) shows both split Ba(2) sites, however only one is occupied at a time. Ba(2) and Ge(6) are located on the 3-fold axis of the unit cell. In the case of Ba(2) site the lines mark the shortest Ba(2)-Ge(3) bonds.

Fig. 6 The Ba(1)-Ge(3), Ba(1)-Ge(4) and Ba(1)-Ge(6) distances in $\text{Ba}_6\text{Ge}_{25}$ as functions of temperature. The lines are guide for eye.

Fig. 7 The length of the Ba(1) and Ba(2) cages along the 3-fold axis in $\text{Ba}_6\text{Ge}_{25}$ as a function of temperature. The lines are guide for eye.

Fig. 8 The Ba(2)-Ba(2) and Ba(3)-Ba(3) split site distance in $\text{Ba}_6\text{Ge}_{25}$ as a function of temperature. The error bars represent the standard deviation obtained from refinement. The lines are guide for eye.

Fig. 9 Local environment of Ba(3) site in $\text{Ba}_6\text{Ge}_{25}$ at 20K derived from Rietveld refinement. Ba(2) atoms from neighbouring cages are also shown. This cage has 2-fold symmetry, the rotation axis intercepts the Ge(1)-Ge(1) and Ge(4)-Ge(4) bonds in the middle. Only one Ba(3) site is occupied at a time.

Fig. 10 The Ba(2)-Ba(2) split site distance as a function of Ba(3)-Ba(3) split site distance in $\text{Ba}_6\text{Ge}_{25}$. The solid line is a linear fit as discussed in the text.

Fig. 11 The Ba(2)-Ba(3) shortest distance in $\text{Ba}_6\text{Ge}_{25}$ as a function of temperature. The line is a guide for eye.

Fig. 12 The quadric double well potential used to demonstrate thermal de-trapping of barium atoms in double-site cages. The potential is bound on both sides by infinite walls, V_0 denotes the height of potential barrier.

TABLE I: Refined lattice constant and fractional coordinates of atoms in Ba₆Ge₂₅ at 20K and 300K. S.G. $P4_132$: Ba(1) 8c (x,x,x); Ba(2) 8c (x,x,x); Ba(3) 24e (x,y,z); Ge(1) 24e (x,y,z); Ge(2) 12d (y,y+1/4,1/8); Ge(3) 24e (x,y,z); Ge(4) 8c (x,x,x); Ge(5) 24e (x,y,z); Ge(6) 8c (x,x,x).

Atom	20 K			300 K		
	x	y	z	x	y	z
Ba(1)	0.0642(4)	0.0642(4)	0.0642(4)	0.0618(3)	0.0618(3)	0.0618(3)
Ba(2)	0.3606(6)	0.3606(6)	0.3606(6)	0.3670(8)	0.3670(8)	0.3670(8)
Ba(3)	0.1867(6)	0.4418(7)	0.1539(5)	0.1893(6)	0.4404(7)	0.1443(5)
Ge(1)	1.0005(2)	0.2974(1)	0.0428(2)	0.9988(2)	0.2970(1)	0.0419(1)
Ge(2)	0.8320(2)	0.0820(2)	1/8	0.8307(1)	0.0807(1)	1/8
Ge(3)	0.8534(2)	0.9142(2)	0.0836(2)	0.8520(1)	0.9153(2)	0.0834(2)
Ge(4)	0.9240(2)	0.9240(2)	0.9240(2)	0.9240(2)	0.9240(2)	0.9240(2)
Ge(5)	0.1270(2)	0.2588(2)	0.9350(2)	0.1264(2)	0.2597(2)	0.9345(2)
Ge(6)	0.2169(2)	0.2169(2)	0.2169(2)	0.2181(2)	0.2181(2)	0.2181(2)
	a [Å]	R _{wp}	R _p	a [Å]	R _{wp}	R _p
	14.52828(8)	0.0651	0.0641	14.54536(7)	0.0524	0.0508

TABLE II: Refined thermal parameters of atoms in Ba₆Ge₂₅ at 20K and 300K in [Å²]. Ba(2) and Ba(3) thermal factors were refined using an isotropic model ($U_{iso}=U_{11}$).

T [K]	Atom	100U ₁₁	100U ₂₂	100U ₃₃	100U ₁₂	100U ₁₃	100U ₂₃
20	Ba(1)	1.0(1)	1.0(1)	1.0(1)	1.3(2)	1.3(2)	1.3(2)
20	Ba(2)	2.5(4)	2.5	2.5	0.0	0.0	0.0
20	Ba(3)	1.8(2)	1.8	1.8	0.0	0.0	0.0
20	Ge(1)	-0.2(1)	0.2(2)	1.7(2)	-0.4(1)	0.5(1)	-0.5(1)
20	Ge(2)	2.1(2)	2.1(2)	3.3(3)	1.0(3)	1.0(2)	-1.0(2)
20	Ge(3)	-1.4(1)	1.9(2)	1.0(1)	-0.4(1)	-0.1(1)	0.7(1)
20	Ge(4)	0.0(1)	0.0(1)	0.0(1)	0.3(1)	0.3(1)	0.3(1)
20	Ge(5)	-0.2(1)	-0.2(2)	1.1(2)	-0.2(1)	0.1(1)	0.6(1)
20	Ge(6)	2.5(2)	2.5(2)	2.5(2)	0.5(2)	-0.5(2)	-0.5(2)
300	Ba(1)	1.3(1)	1.3(1)	1.3(1)	0.9(2)	0.9(2)	0.9(2)
300	Ba(2)	3.3(4)	3.3	3.3	0.0	0.0	0.0
300	Ba(3)	2.2(2)	2.2	2.2	0.0	0.0	0.0
300	Ge(1)	-0.1(1)	1.3(2)	1.3(1)	0.4(1)	0.3(1)	-0.1(1)
300	Ge(2)	1.0(1)	1.0(1)	1.0(2)	0.7(2)	0.1(1)	-0.1(1)
300	Ge(3)	0.3(1)	0.7(1)	1.7(1)	-0.5(1)	0.31(9)	0.1(1)
300	Ge(4)	0.73(9)	0.73(9)	0.73(9)	0.0(1)	0.0(1)	0.0(1)
300	Ge(5)	0.7(1)	0.5(1)	1.2(1)	-0.10(9)	-0.1(1)	0.4(1)
300	Ge(6)	2.6(1)	2.6(1)	2.6(1)	0.4(1)	-0.4(1)	-0.4(1)

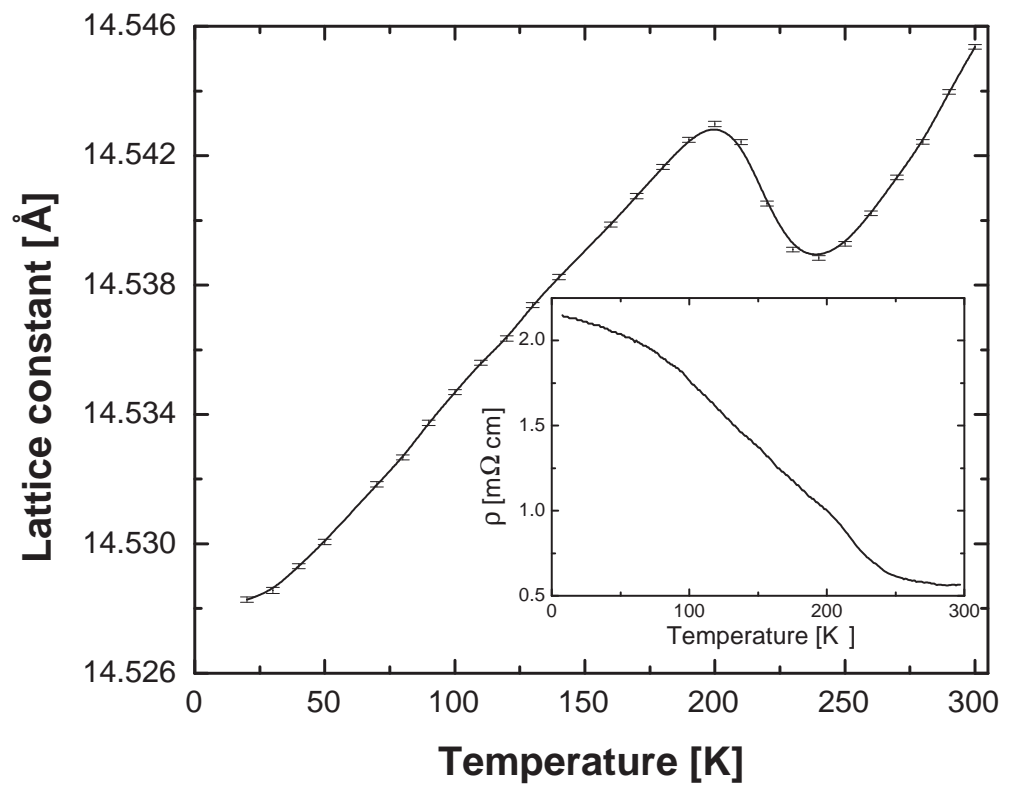


Figure 1, M. Schmidt, Phys. Rev. B

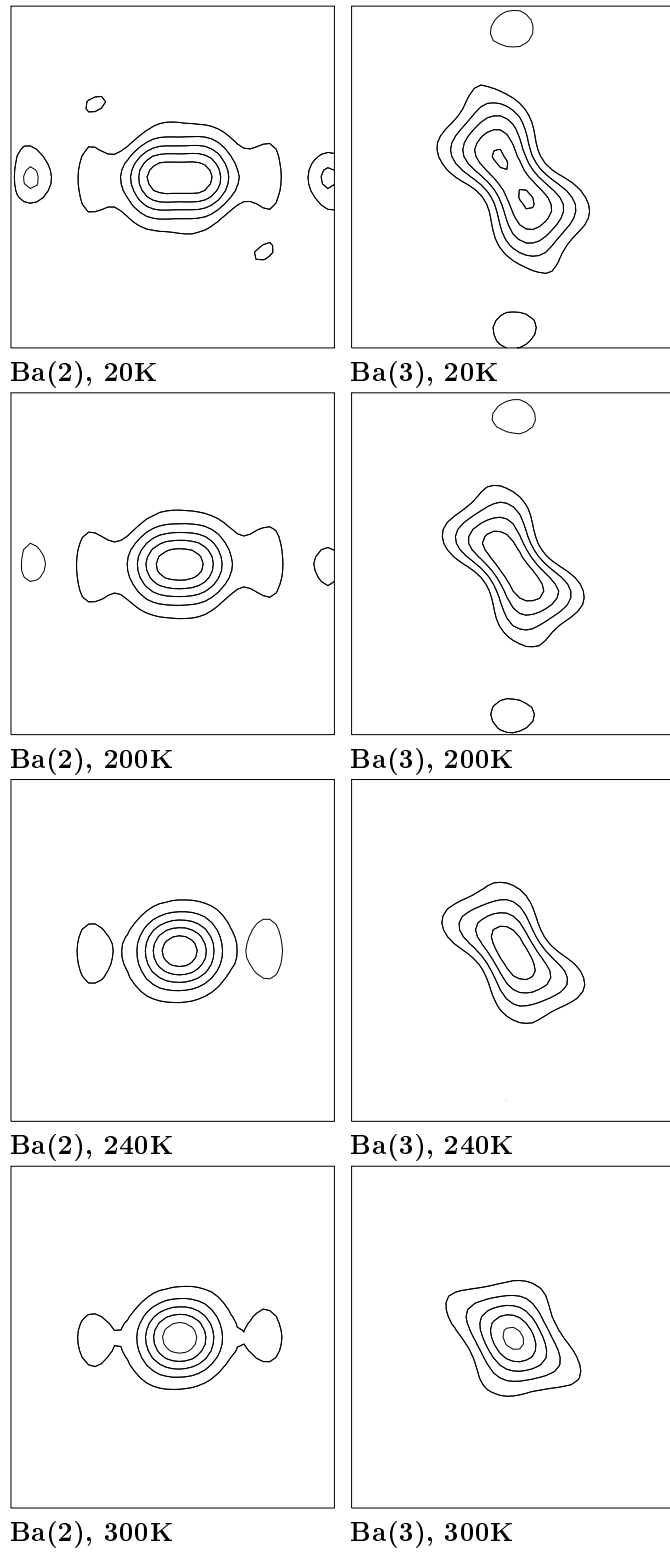


Figure 2, M. Schmidt, Phys. Rev. B

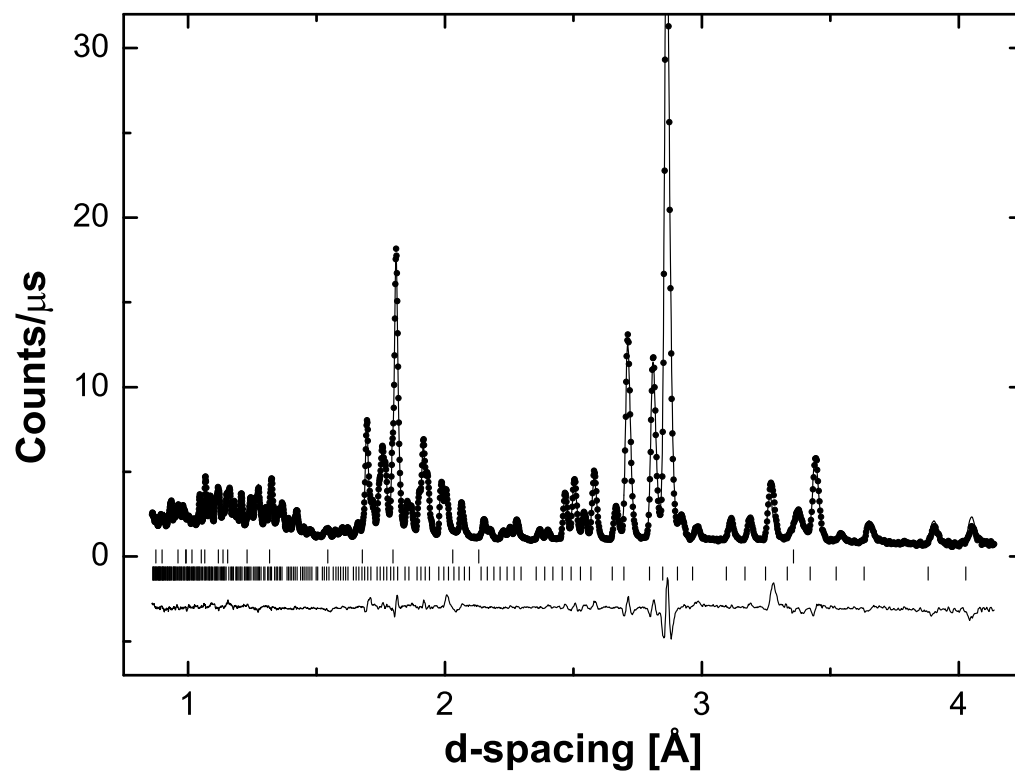


Figure 3, M. Schmidt, Phys. Rev. B

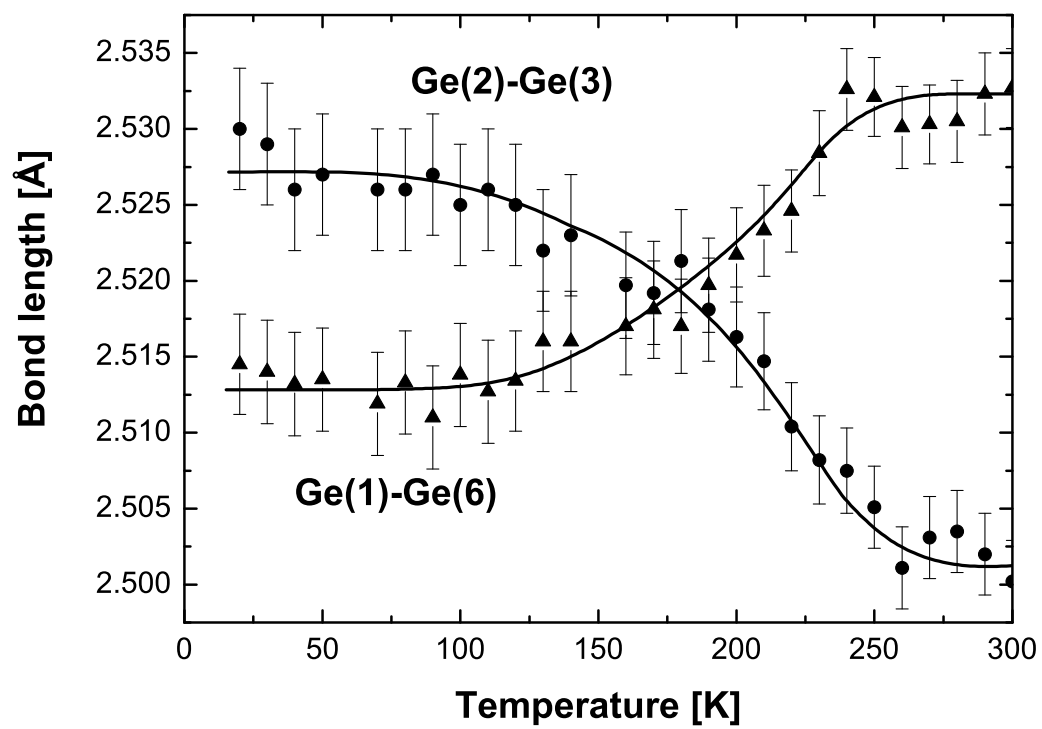
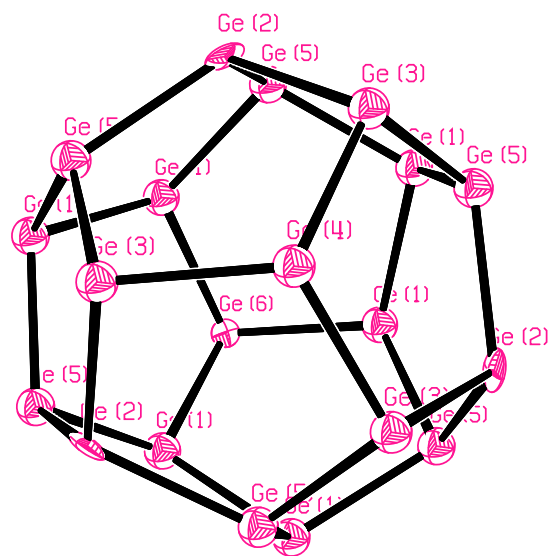
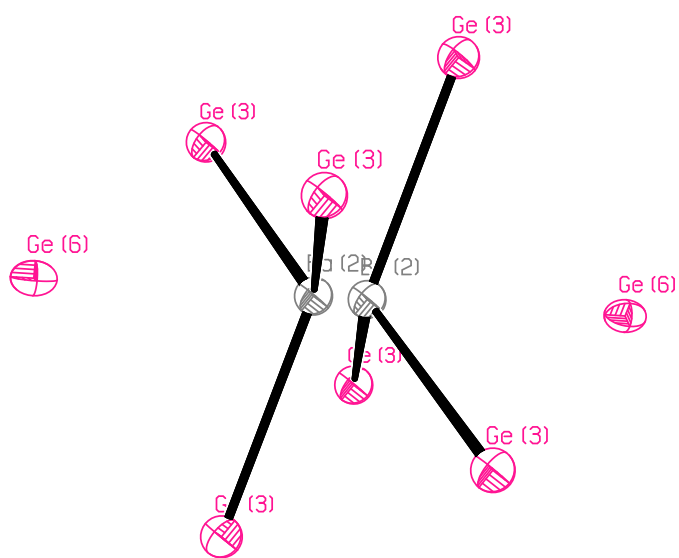


Figure 4, M. Schmidt, Phys. Rev. B



Ba(1)



Ba(2)

Figure 5, M. Schmidt, Phys. Rev. B

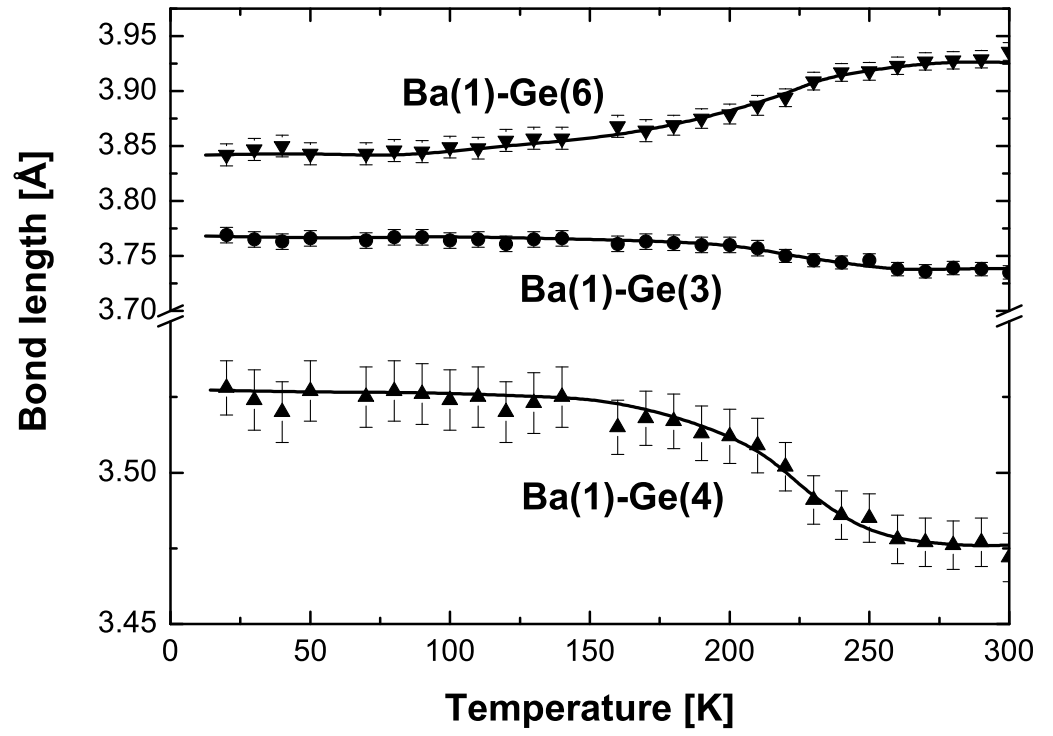


Figure 6, M. Schmidt, Phys. Rev. B

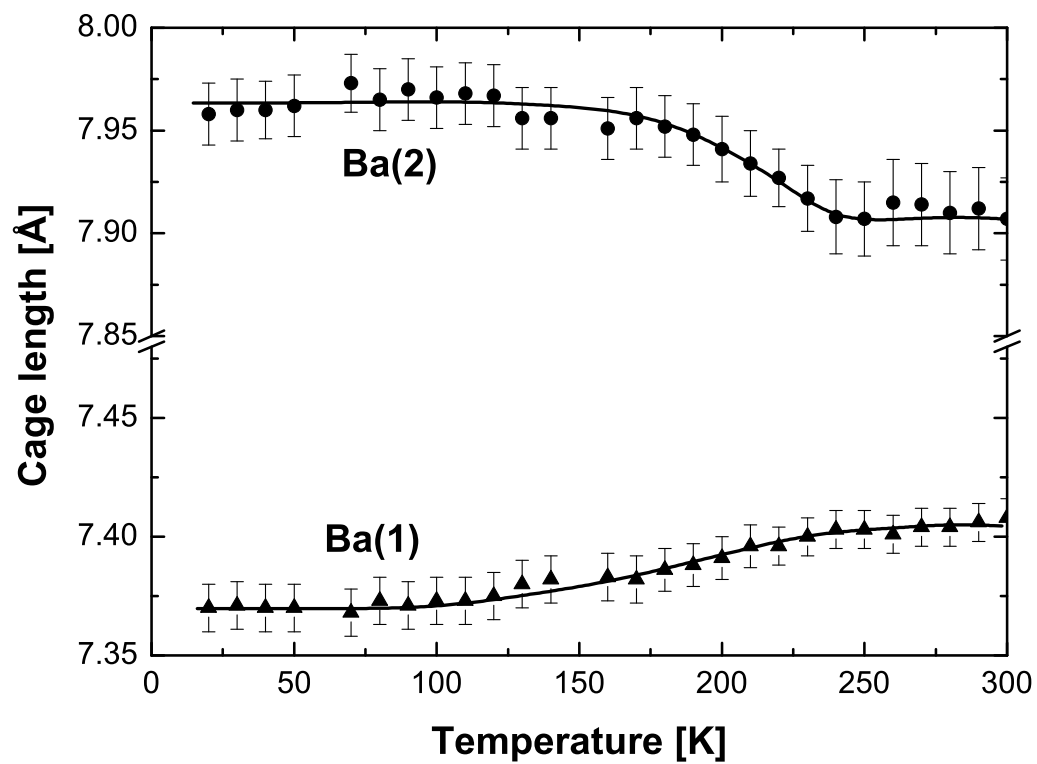


Figure 7, M. Schmidt, Phys. Rev. B

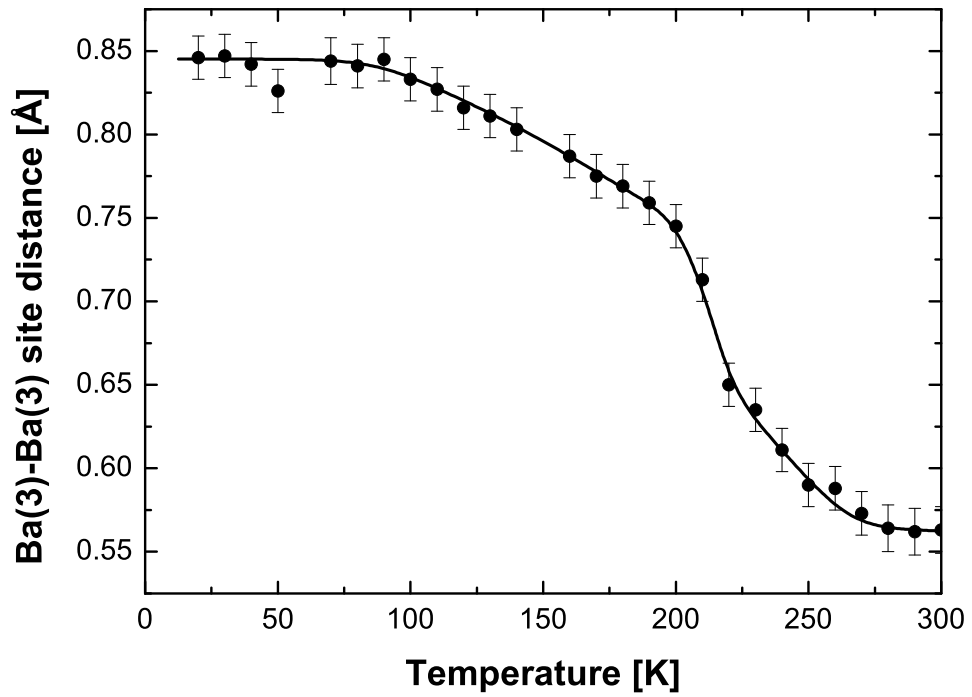
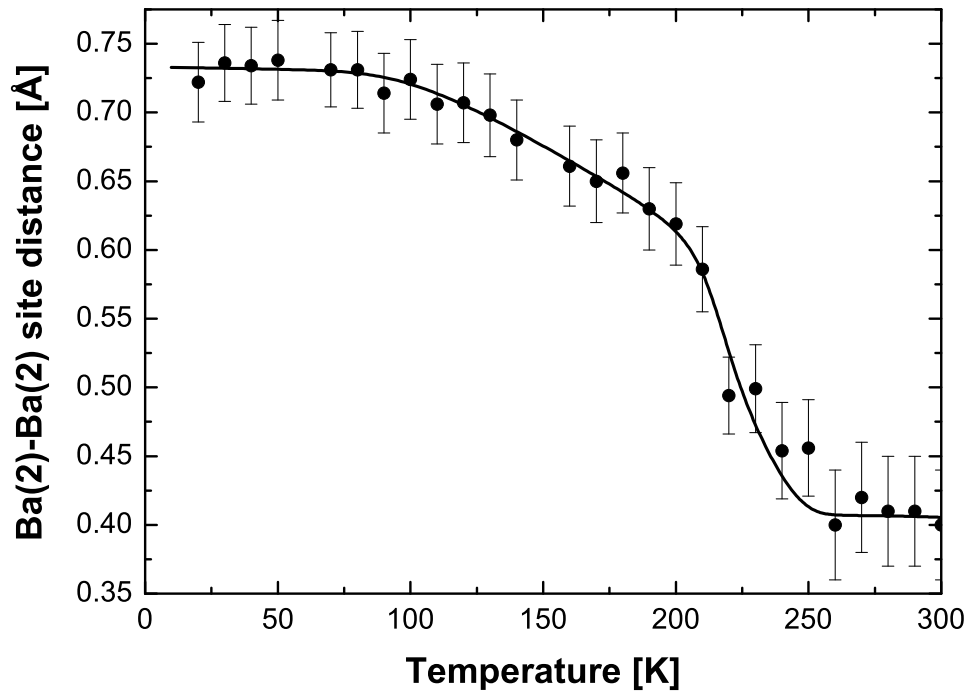


Figure 8, M. Schmidt, Phys. Rev. B

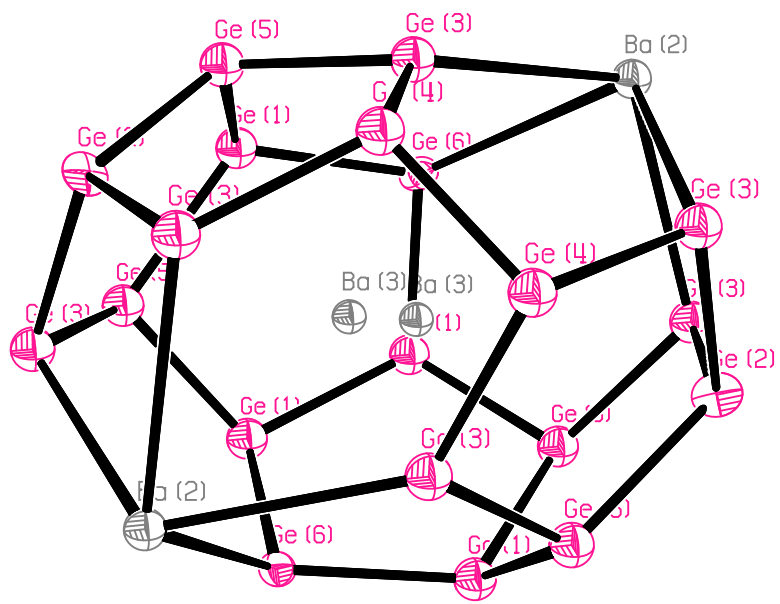


Figure 9, M. Schmidt, Phys. Rev. B

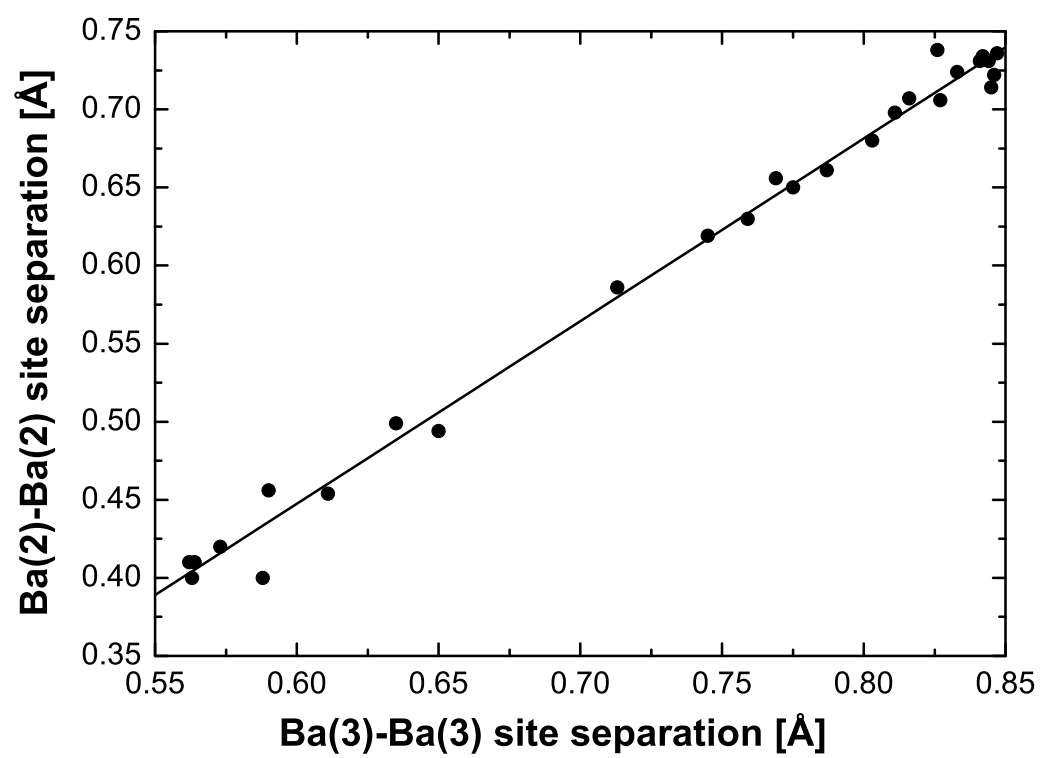


Figure 10, M. Schmidt, Phys. Rev. B

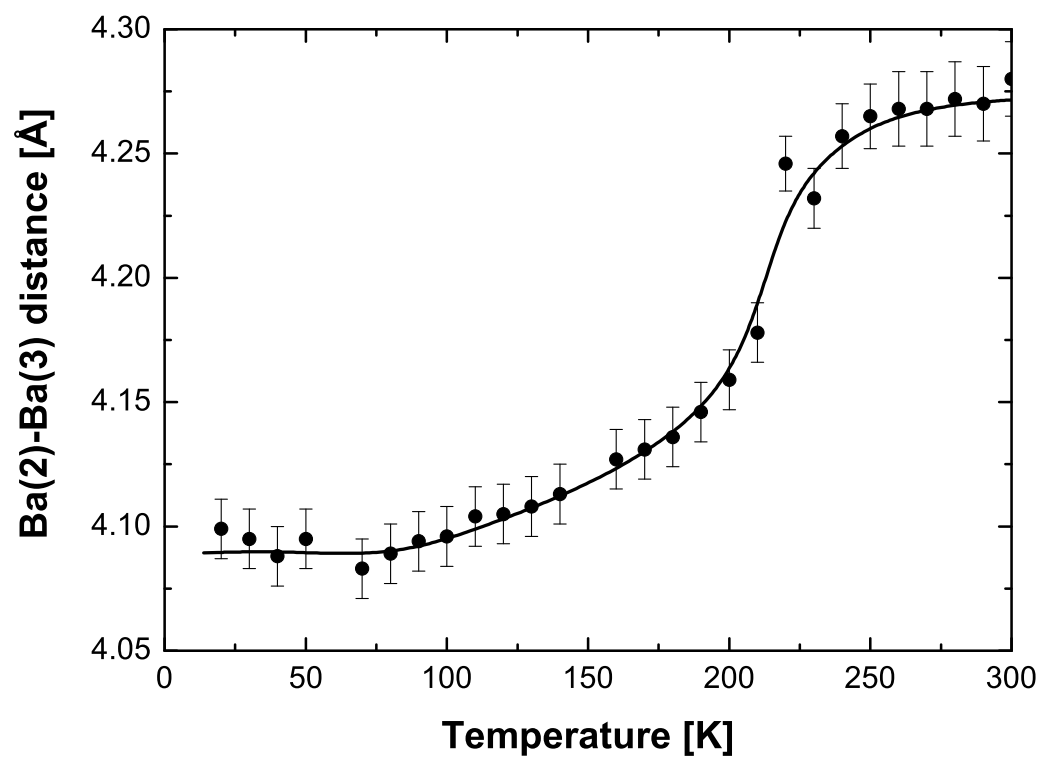


Figure 11, M. Schmidt, Phys. Rev. B

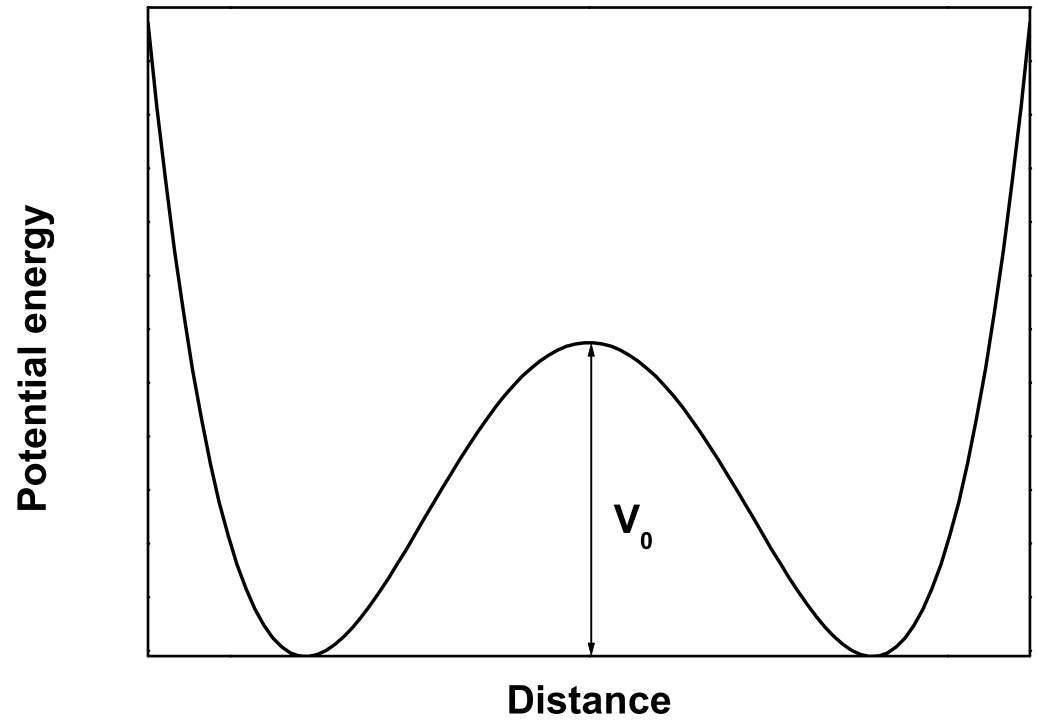


Figure 12, M. Schmidt, Phys. Rev. B